The Astrophysical Journal, 956:121 (13pp), 2023 October 20 https://doi.org/10.3847/1538-4357/ace970


# X-Rays Trace the Volatile Content of Interstellar Objects

Samuel H. C. Cabot[1], Q. Daniel Wang[2], and Darryl Z. Seligman[3,4]
[1] Yale University, 52 Hillhouse, New Haven, CT 06511, USA; sam.cabot@yale.edu
[2] Astronomy Department, University of Massachusetts, Amherst, MA 01003, USA
[3] Department of Astronomy and Carl Sagan Institute, Cornell University, 122 Sciences Drive, Ithaca, NY 14853, USA
*Received 2022 June 10; revised 2023 July 18; accepted 2023 July 19; published 2023 October 13*

## Abstract

The nondetection of a coma surrounding 1I/'Oumuamua, the first discovered interstellar object (ISO), has prompted a variety of hypotheses to explain its nongravitational acceleration. Given that forthcoming surveys are poised to identify analogs of this enigmatic object, it is prudent to devise alternative approaches to characterization. In this study, we posit X-ray spectroscopy as a surprisingly effective probe of volatile ISO compositions. Heavily ionized metals in the solar wind interact with outgassed neutrals and emit high-energy photons in a process known as charge exchange, and charge-exchange-induced X-rays from comets and planetary bodies have been observed extensively in our solar system. We develop a model to predict the X-ray flux of an ISO based on its chemical inventory and ephemeris. We find that while standard cometary constituents, such as $H_2O$, $CO_2$, CO, and dust, are best probed via optical or infrared observations, we predict strong X-ray emission generated by charge exchange with extended comae of $H_2$ and $N_2$—species that lack strong infrared fluorescence transitions. We find that XMM-Newton would have been sensitive to charge exchange emission from 1I/'Oumuamua during the object's close approach to Earth, and that constraints on composition may have been feasible. We argue for follow-up X-ray observations of newly discovered ISOs with close-in perihelia. Compositional constraints on the general ISO population could reconcile the apparently self-conflicting nature of 1I/'Oumuamua and provide insight into the earliest stages of planet formation in extrasolar systems.

*Unified Astronomy Thesaurus concepts:* Interstellar objects (52); X-ray sources (1822); Comae (271); Solar wind (1534)

## 1. Introduction

Knowledge of the compositions of minor bodies has considerably influenced our understanding of the early solar system. While investigations of their dynamical histories are limited by the solar system's chaotic nature (Wisdom 1980; Laskar 1989; Batygin & Laughlin 2008; Laskar & Gastineau 2009), compositional measurements of minor bodies—especially of their interiors—have the potential to reveal their formation environments (Öberg et al. 2011).

Remarkably, the solar system likely ejected tens of earth masses of volatile rich material during the early stages of its formation and evolution (Hahn & Malhotra 1999; Gomes et al. 2004; Morbidelli et al. 2005; Tsiganis et al. 2005; Levison et al. 2008; Raymond et al. 2018, 2020). Therefore, it is reasonable to expect that extrasolar planetary systems contribute to a galactic population of interstellar comets, and that some will encounter the solar system on hyperbolic trajectories (Moro-Martín et al. 2009; Cook et al. 2016; Engelhardt et al. 2017). Naturally, it came as a surprise that 1I/'Oumuamua, the first discovered interstellar object (ISO), exhibited none of the typical properties of solar system comets (for recent reviews, see Jewitt & Seligman 2023; Moro-Martín 2022). It had no visible coma (Jewitt et al. 2017; Meech et al. 2017; Bolin et al. 2018; Trilling et al. 2018), an extreme shape (e.g., Knight et al. 2017; Mashchenko 2019), a reddened reflection spectrum (Masiero 2017), a young dynamical age (e.g., Mamajek 2017; Hsieh et al. 2021), and nonzero nongravitational acceleration (Micheli et al. 2018).

The second discovered ISO, 2I/Borisov, was unambiguously a comet (Jewitt & Luu 2019), perhaps more in line with expectations. Its cometary activity was readily measured and typical carbon- and nitrogen-bearing species were detected (Opitom et al. 2019; Bannister et al. 2020; Kareta et al. 2020; Lin et al. 2020; Xing et al. 2020; Aravind et al. 2021). Atacama Large Millimeter/submillimeter Array and Hubble observations revealed that it was enriched in CO relative to $H_2O$ (Bodewits et al. 2020; Cordiner et al. 2020). This finding suggests that 2I/Borisov formed exterior to the CO snowline in the protoplanetary disk (Price et al. 2021; Seligman et al. 2022) of a very young (Lisse et al. 2022) or a very carbon-enriched system (see Bodewits et al. 2020).

1I/'Oumuamua's former provenance remains in question, and dynamically backtracing either ISO to their respective host systems is difficult (Mamajek 2017; Bailer-Jones et al. 2018). 1I/'Oumuamua's peculiar properties and elusiveness to follow-up spectroscopy have prompted a variety of theories regarding its origin. If the measured nongravitational acceleration was driven by cometary outgassing, this would be energetically consistent with a composition of $H_2$ (Füglistaler & Pfenniger 2018; Seligman & Laughlin 2020; Levine & Laughlin 2021), $N_2$ (Desch & Jackson 2021; Jackson & Desch 2021), or CO (Seligman et al. 2021). Confirming an $H_2$ or $N_2$ composition would have immediately revealed a new mechanism of generating minor bodies: formation in the cores of molecular clouds (Seligman & Laughlin 2020) or ejection of ice from the surfaces of Pluto analogs due to impact events (Desch & Jackson 2021). Alternatively, if the acceleration was caused by

[4] NSF Astronomy and Astrophysics Postdoctoral Fellow.

radiation pressure (Micheli et al. 2018), then 1I/'Oumuamua must have been extremely porous (Flekkøy et al. 2019; Moro-Martín 2019; Sekanina 2019; Luu et al. 2020) or thin (Bialy & Loeb 2018). While $H_2O$, $CO_2$, and CO species in cometary comae are easily measured via infrared spectroscopy, the possible presence of difficult to detect homonuclear $H_2$ or $N_2$ prompts a search for alternative methods for characterizing interstellar comets.

This study presents such a new approach: X-ray observations of solar wind (SW) charge exchange (CX). X-ray observations of an ISO should immediately reveal the presence of an outgassed coma. CX involves the transfer of electrons from a cool neutral medium to heavily ionized metals in the SW. Following the unexpected detection of X-rays emanating from C/1996 B2 (Hyakutake; Lisse et al. 1996; Cravens 1997), CX has been observed with a multitude of other comets (Dennerl et al. 1997; Lisse et al. 1999; Cravens 2000, 2002; Lisse et al. 2004; Bodewits et al. 2007). CX conveys information about the composition and speed of the SW (Beiersdorfer et al. 2001; Bodewits et al. 2007; Gu et al. 2016). Studies have also linked CX emission to physical and chemical properties of the minor body and its coma through the morphology of the X-ray emission profile (Wegmann et al. 2004) and emission line ratios (Mullen et al. 2017).

Indeed, there are encouraging prospects for discovering additional ISOs in the coming decade. Population synthesis models of the galactic population of ISOs have demonstrated that the Rubin Observatory Legacy Survey of Space and Time will detect 1–2 1I/'Oumuamua analogs every year (Hoover et al. 2022).

This paper is organized as follows. In Section 2, we discuss the advantages and limitations of X-ray observations for characterizing minor bodies and outline a simple model of CX emission. We apply our model to 1I/'Oumuamua and 2I/Borisov in Section 3 and compare our predictions to the known correlation between X-ray and visible-band flux. Our model suggests that if 1I/'Oumuamua did indeed outgas a coma, that CX would have been detectable with current-generation X-ray facilities during the period that it approached Earth. Section 4 establishes expectations for detecting CX with new ISOs discovered by the Rubin Observatory. Finally, our conclusions are summarized in Section 5. We refer the reader to Appendix A for a brief review of CX fundamentals and to Appendix B for the details of our CX model.

## 2. Motivation and Model

This section establishes use cases for X-ray observations of ISOs and sets forth an analytic model of X-ray emission from outgassed comae. It also specifies the traits of ISOs (i.e., bulk composition and orbital trajectory) from which we expect robust detection of X-ray emission with present-day facilities.

### 2.1. Information Gained from X-Ray Observations

As a primer, it is useful to review the prototypical case of CX from an outgassed coma: C/1996 B2 (Hyakutake), a long-period comet that came within 0.23 au of the Sun at perihelion. Infrared observations yielded unambiguous detections of $H_2O$, CO, $CH_4$, and $C_2H_6$ (Mumma et al. 1996; Dello Russo et al. 2002). Contemporaneously, significant X-ray emission was detected out to ~100,000 km ($6.7 \times 10^{-4}$ au) from its nucleus by Lisse et al. (1996). CX was suggested as the responsible process by Cravens (1997) and reaffirmed by Wegmann et al. (1998). Other mechanisms (e.g., thermal bremsstrahlung, scattering, and fluorescence) may be ruled out (Krasnopolsky 1997; Lisse et al. 1999, 2004). Since this detection, sophisticated models of CX with cometary comae have been developed, such as the hydrodynamical simulations by Wegmann et al. (2004), and CX has been observed with comae of numerous other comets (e.g., Bodewits et al. 2007; Ewing et al. 2013).

X-rays have conventionally been of limited value for compositional studies of minor bodies. For one, CX detections arise only from significantly extended comae. Moreover, the most immediate insights conveyed are the morphology of the coma and the properties of the SW (Lisse et al. 2004). Infrared/radio spectroscopy remains the de facto technique for detecting molecular species that exhibit solar-pumped fluorescence transitions (Crovisier & Encrenaz 1983; Bockelée-Morvan et al. 2004). Such species (reviewed by, e.g., Biver & Bockelée-Morvan 2016; Bockelée-Morvan & Biver 2017) include $H_2O$, CO, $CO_2$, $CH_4$, $C_2H_2$, $C_2H_6$, and HCN. Complementary to infrared observations, UV spectroscopy can measure the production of some additional species (Biver et al. 2022), such as noble gases and homonuclear diatomic molecules. However, except for a small number of tenuous reports of their sublimation (e.g., Ar in Hale-Bopp; Stern et al. 2000), noble gases remained elusive in comets prior to in situ detections in 67P (Rubin et al. 2018) by the European Space Agency's Rosetta mission. Rosetta also confirmed the presence $O_2$ and $N_2$ in comets (Bieler et al. 2015; Rubin et al. 2015).

This study explores a novel use case for X-ray observations: to reveal an outgassed coma that is invisible in the infrared and that may arise from the perihelion passage of an ISO. While the composition of 1I/'Oumuamua remains debated, a number of candidate species (Table 1) are monotomic or homonuclear diatomic and will not fluoresce in the infrared. However, CX will occur at a neutral medium, even one that does not produce observable thermal emission, fluorescence, or scattering. Therefore, the outgassed coma of an ISO may be X-ray-bright even in the absence of infrared and optical detections. In particular, X-ray observations offer a promising avenue for

**Table 1**
Cryogenic Chemical Properties for Volatiles That May Be Constituents of ISOs

| Species | $T_{Sub}$ (K) | $\gamma$ | $\Delta H$ (kJ mole$^{-1}$) | $c_s$ (km s$^{-1}$) | $\mathcal{H}$ (kJ $\times 10^{-23}$) |
|---|---|---|---|---|---|
| $H_2$ | 6 | 7/5 | 1 | 0.19 | 0.18 |
| Ne | 9 | 5/3 | 1.9 | 0.11 | 0.34 |
| $N_2$ | 25 | 7/5 | 7.34 | 0.14 | 1.27 |
| CO | 58 | 7/5 | 7.6 | 0.15 | 1.37 |
| Ar | 30 | 5/3 | 7.79 | 0.15 | 1.36 |
| $O_2$ | 30 | 7/5 | 9.26 | 0.10 | 1.60 |
| Kr | 40 | 5/3 | 11.53 | 0.12 | 2.01 |
| Xe | 55 | 5/3 | 15.79 | 0.12 | 2.75 |
| $CO_2$ | 82 | 8/6 | 28.84 | 0.14 | 4.94 |
| $H_2O$ | 155 | 8/6 | 54.46 | 0.31 | 9.33 |

**Notes.** For each species, we report the temperature of sublimation ($T_{Sub}$), ideal adiabatic index ($\gamma$), enthalpy of sublimation ($\Delta H$), and sound speed ($c_s$) per Equation (B10). We also report the total energy input to a single particle ($\mathcal{H}$) per Equation (B9). The data are from Shakeel et al. (2018), except those for CO, which were obtained from Stephenson & Malanowski (1987) and the NIST database.

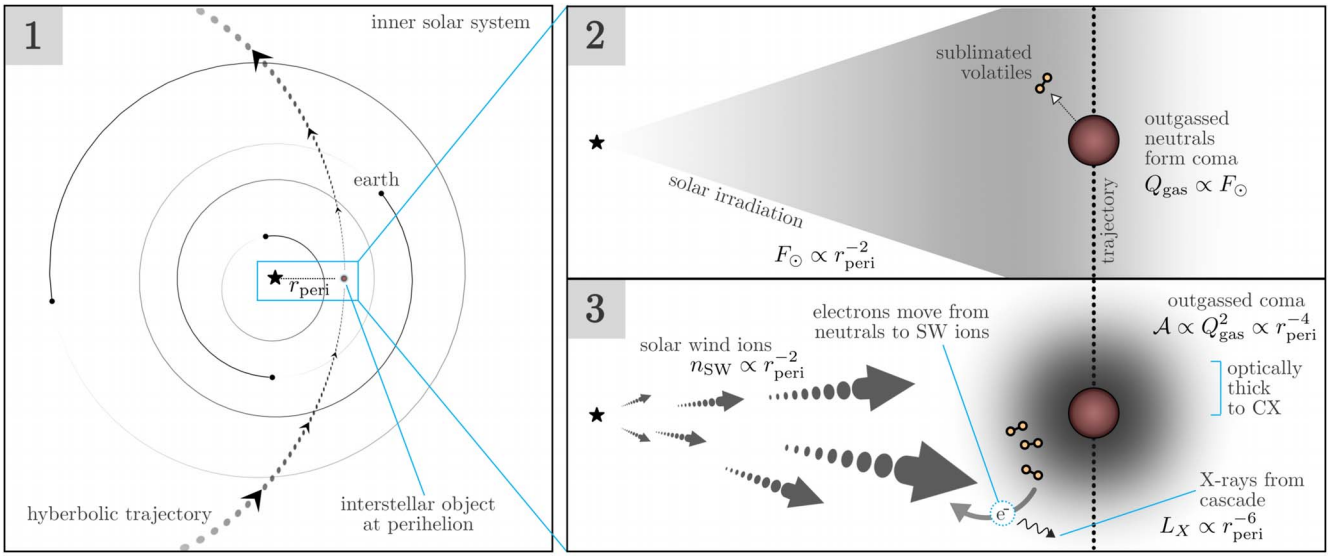


**Figure 1.** Schematic of SW CX with the outgassed neutrals in the coma of an ISO. Panel 1: an instantaneous view of the inner solar system and the trajectory of an ISO, currently at perihelion ($r_{peri}$). Panel 2: the flux of solar radiation ($F_\odot$) heats the volatiles on the ISO's surface, which causes the sublimation and outgassing of neutral volatiles at a rate $Q_{gas}$. Panel 3: SW ions (with number density $n_{SW}$) interact with the outgassed coma through CX. Electrons are transferred from the neutral coma to the bare or H-like SW ions and the subsequent cascade emits X-rays. The coma's interaction cross section ($\mathcal{A}$) scales with $Q_{gas}^2$. As a result, the X-ray luminosity follows $L_X \propto r_{peri}^{-6}$ (Equation (5); Section 2.2).

remote sensing an $H_2$ or $N_2$ coma. Both of these species are thermodynamically consistent with 1I/'Oumuamua's nongravitational acceleration under outgassing and comprise the focus of this study. Per Seligman et al. (2021), we benchmark results to a CO composition (c.f. Trilling et al. 2018), although this molecule is more readily detected in the infrared.

### 2.2. Scaling Relationships

In Appendix B, we develop a model that links X-ray flux to a minor body's physical properties. Specifically, it depends on the following key parameters: the neutral production rate ($Q_{gas}$), mean radius of the nucleus ($a$), perihelion distance ($r_{peri}$), sublimation + kinetic energy of the relevant volatiles ($\mathcal{H}$), geocentric distance ($\Delta_e$), SW number density ($n_{SW}$), CX interaction area of the coma ($\mathcal{A}$), X-ray luminosity ($L_X$), and flux ($F_X$). The pertinent relationships are as follows:

$$Q_{gas} \propto a^2 r_{peri}^{-2} \mathcal{H}^{-1}, \quad (1)$$

$$\mathcal{A} \propto Q_{gas}^2 \text{ (to leading order)}, \quad (2)$$

$$n_{SW} \propto r_{peri}^{-2}, \quad (3)$$

$$L_X \propto n_{SW} \mathcal{A}, \quad (4)$$

$$F_X \propto \Delta_e^{-2} L_X \propto a^4 r_{peri}^{-6} \mathcal{H}^{-2} \Delta_e^{-2}. \quad (5)$$

In our model, constants of proportionality are calibrated to measurements of C/1996 B2 (Hyakutake; Lisse et al. (1996); Appendix B). The above scaling relationships demonstrate that the X-ray brightness of a minor body can be significantly enhanced by a close-in perihelion passage and a particularly volatile composition. Figure 1 shows a schematic of such an ISO encounter, where the scaling relationships and underlying physical processes are depicted in the individual panels.

### 2.3. Detection Thresholds

In this section, we gauge the feasibility of detecting CX with an outgassed coma, including the requisite X-ray flux and exposure durations. Our predictions are for the EPIC pn detector on board XMM-Newton, which has the advantage of a larger effective area (approximately $A = 900$ cm$^2$ at 0.5 kev) compared to the other space-based X-ray detectors. To estimate the detectability of a comet or ISO, one needs to account for the noise contribution from the background, which is chiefly made of background active galactic nuclei and the diffuse hot plasma emission from the general interstellar and circumgalactic media of the galaxy, the Local Bubble, and SW CX emission within the heliosphere (e.g., McCammon et al. 2002; Koutroumpa 2012). Based on archival blank-sky EPIC pn observations, we estimate that the total background intensity is $\Sigma = 1.4 \times 10^{-3}$ counts s$^{-1}$ arcmin$^{-2}$ in the 0.5–0.7 keV band, for example, which encloses the typically strong O VII and O VIII K$\alpha$ lines. The total background intensity also includes the contribution from non-X-ray (cosmic-ray-induced) instrument events. Let $\Phi_X$ denote the X-ray flux at the detector due to CX with the target (units of counts s$^{-1}$ cm$^{-2}$) and let $\tau$ denote the exposure duration. Furthermore, we assume that nearly all of the signal is contained within a solid angle $\Omega$ for simplicity. Then the signal-to-noise ratio (S/N) of the CX signature is

$$S/N = \Phi_X A \sqrt{\tau} / \sqrt{\Phi_X A + \Sigma \Omega}. \quad (6)$$

Alternatively, this equation can also be rearranged into an expression for $\tau$ for a desired S/N threshold.

One caveat is that a continuous exposure may be ineffective for fast-moving targets. Photon events may, however, be spatially calibrated across discrete slews that keep the object on the focal plane array (FPA). This enables multiple on-target pointings and the reconstruction of events in the cometocentric frame based on the attitude of the telescope. The maximum exposure duration for any one pointing is then limited by the field of view of the telescope and the angular velocity of the target. For reference, 1I/'Oumuamua's angular velocity reached $1.4 \times 10^{-4}$ deg s$^{-1}$ at its closest approach to Earth. The crossing time for XMM-Newton's $30' \times 30'$ field of view would have been up to ~3.5 ks.

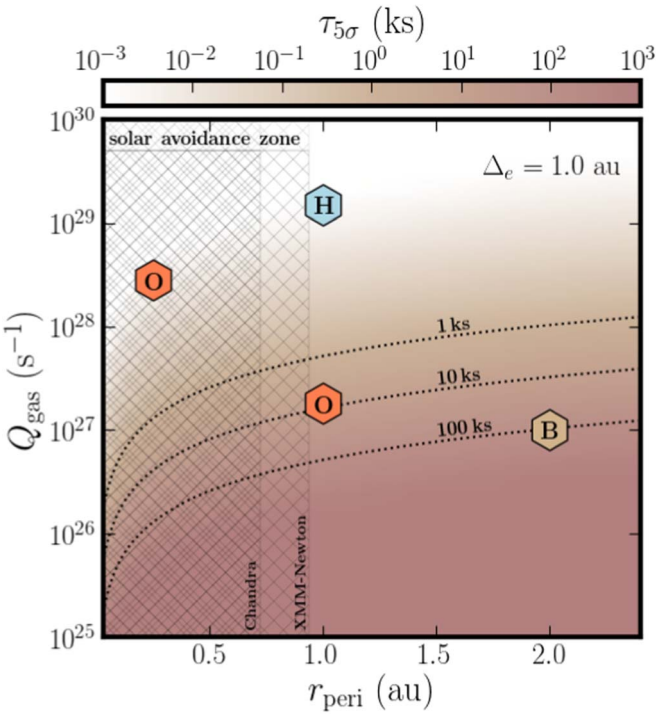


**Figure 2.** Exposure time (ks) required for a $5\sigma$ detection of CX X-ray emission (Equation (B12)), as a function of the outgassing rate $Q_{\rm gas}$ and perihelion distance $r_{\rm peri}$. The geocentric distance is fixed at $\Delta_e = 1$ au. The background rate and effective area correspond to those of EPIC pn on XMM-Newton. For reference, the markers are plotted at locations representative of real minor bodies: light blue ("H") corresponds to $Q_{\rm gas} = 1.5 \times 10^{29}$ $\rm s^{-1}$ observed at 1.0 au—similar to C/1996 B2 (Hyakutake); tan ("B") corresponds to $Q_{\rm gas} = 10^{27}$ $\rm s^{-1}$ observed at 2.0 au—similar to 2I/Borisov; and coral ("O") corresponds to $Q_{\rm gas} = 2.8 \times 10^{28}$ $\rm s^{-1}$ observed at 0.25 au and $Q_{\rm gas} = 1.8 \times 10^{27}$ $\rm s^{-1}$ observed at 1.0 au—estimates corresponding to 1I/'Oumuamua under a CO composition. The solar elongation angles of Chandra ($\psi_\odot^{min} = 46.4°$) and XMM-Newton ($\psi_\odot^{\rm min} = 70°$) impose lower bounds ($\sin \psi_\odot^{\rm min}$) on observable $r_p$, and their respective restricted zones are hatched in the figure. The lower bound is attained only in the ideal orbital case and observable heliocentric distances are typically significantly larger due to spacecraft limitations.

Space-based X-ray observatories have minimum solar elongation angles ($\psi_\odot^{\rm min}$) for reasons pertaining to detector safety (e.g., avoiding burnout incidents similar to ROSAT's), thermal stability, and power supply. For Chandra, $\psi_\odot^{\rm min} = 46.^\circ 4$, and for XMM-Newton, $\psi_\odot^{\rm min} = 70°$. These constraints permit observations of small bodies at $R \geqslant 0.72$ au and $R \geqslant 0.94$ au, respectively. These lower bounds can only be attained under optimal alignment between Earth and the object. Future missions will likely have similar safety exclusion zones to protect equipment at the FPA.

Figure 2 depicts the exposure times necessary to achieve S/N = 5 as a function of $Q_{\rm gas}$ and $r_{\rm peri}$, specifically for the XMM-Newton pn detector. For simplicity, the geocentric distance is assumed $\Delta_e = 1$ au. The X-ray luminosity of the CX is given by Equation (B12), and the angular extent of the emission is set by $\tilde{b}$ (Equation (B7)). The markers in Figure 2 are located at the outgassing rates and perihelia of real minor bodies (the outgassing rate of 1I/'Oumuamua was not directly measured, but is estimated in Section 3).

This figure immediately conveys the feasibility of detecting CX emission from outgassed comae with currently operational facilities. For modest exposure times of order 10 ks, CX should be detectable when $Q > 10^{27}$ $\rm s^{-1}$ over a range of $r_{\rm peri}$. Qualitatively, this finding is consistent with previous high-significance ROSAT detections of CX with six comets (Dennerl et al. 1997), whose outgassing rates were between $Q_{\rm gas} = 2 \times 10^{27} - 9 \times 10^{29}$ $\rm s^{-1}$. The heliocentric distances in this sample were between $R = 0.99$ and 1.96 au, and the geocentric distances were between $\Delta_e = 0.12$ and 1.61 au (these comets are discussed further in Section 3.3). While the minor bodies need not be observed at perihelion, our model indicates that $F_{\rm X}$ scales more strongly with heliocentric distance ($R$) than with $\Delta_e$ (Lisse et al. 1999) per Equations (B8) and (B11). As discussed in the next section, 1I/'Oumuamua's proximity to the Earth and Sun would have made it amenable to X-ray observations. On the other hand, 2I/Borisov would have been a more difficult case, because it only came within a minimum 2 au of the Sun.

## 3. Detectability of X-Rays from 2I/Borisov and 1I/'Oumuamua

We proceed to estimate the X-ray luminosity for the only two identified ISOs that traversed our solar system: 1I/'Oumuamua and 2I/Borisov. We first estimate $L_{\rm X}$ using the analytic framework presented in the previous section. We then make an independent estimate based on known trends between optical and X-ray luminosities for comets.

We briefly review the pertinent measurements of both ISOs. From its photometric lightcurve structure, 1I/'Oumuamua is estimated to have had an oblate 6:6:1 ellipsoidal geometry (Mashchenko 2019). Its albedo ($p$) was not constrained, so its true dimensions are uncertain. Meech et al. (2017) and Bolin et al. (2018) measured an effective radius of ~0.1 km, assuming an albedo of 0.04. The lightcurve fit by Mashchenko (2019) yielded dimensions $115 \times 111 \times 19$ m with $p = 0.1$. For our order-of-magnitude calculations, we treat 1I/'Oumuamua as spherical, with radius of $a = 100$ m. However, we emphasize that the true dimensions are albedo-dependent, and the lengths scale as $1/\sqrt{p}$. At perihelion of $r_{\rm peri} = 0.25$ au, 1I/'Oumuamua's distance to Earth was $\Delta_e = 1.23$ au, with an apparent magnitude $V = 21$. The object reached an apparent magnitude of $V = 19.7$ at its closest approach to Earth, with $\Delta_e = 0.16$ au (which also satisfied solar elongation constraints for X-ray observation per Figure 3). Infrared Spitzer observations produced nondetections when 1I/'Oumuamua was outbound at ~2 au, providing upper limits on the production rates of CO or $CO_2$ (Trilling et al. 2018). However, sporadic outgassing of CO might reconcile the nongravitational acceleration and Spitzer nondetection (Seligman et al. 2021).

The nuclear radius of the comet-like 2I/Borisov was constrained to $0.2\,{\rm km} < a < 0.5\,{\rm km}$, based on its brightness profile and nongravitational acceleration, assuming a range of plausible bulk densities (Jewitt & Luu 2019; Bolin et al. 2020). We adopt a nominal radius of $a = 300$ m. Unlike 1I/'Oumuamua, gas emission activity typical of comets was definitely detected from this body. When contemporaneous measurements of $H_2O$ and CO production rates were obtained after perihelion ($r_{\rm peri} = 2$ au), CO dominated the outflow. Specifically, Bodewits et al. (2020) measured $Q({\rm CO}) = 7.5 \times 10^{26}$ $\rm s^{-1}$ at 3.3 days after perihelion and $Q({\rm CO}) = 1.07 \times 10^{27}$ $\rm s^{-1}$ at 22.4 days after perihelion. Also, Cordiner et al. (2020) measured $Q({\rm CO}) = 4.4 \times 10^{26}$ $\rm s^{-1}$ in observations conducted 7–8 days after perihelion. While water production exceeded $Q({\rm H_2O}) = 10^{27}$ $\rm s^{-1}$ prior to perihelion, it dropped below $6 \times 10^{26}$ $\rm s^{-1}$ for observations conducted after perihelion (Bodewits et al. 2020). Jewitt et al. (2020) measured

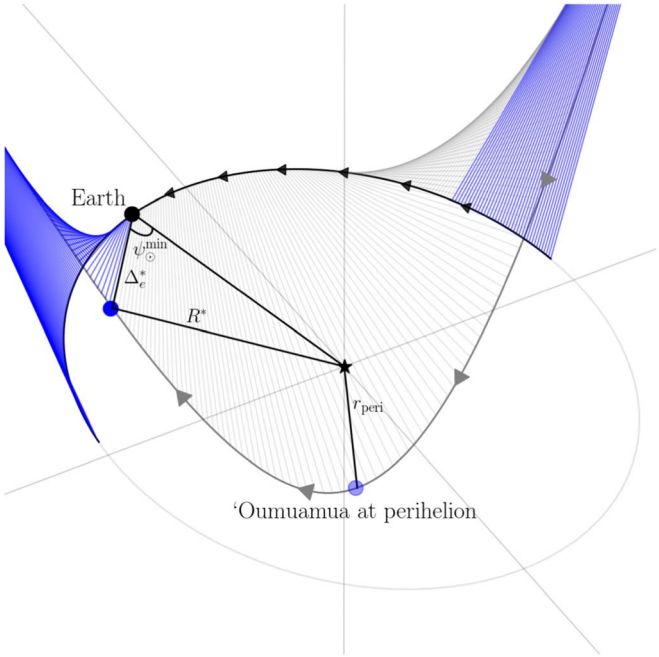


**Figure 3.** Trajectory and X-ray observability of 1I/'Oumuamua, prior to its discovery. The plotted lines connect the instantaneous positions of Earth and 1I/'Oumuamua. The blue lines denote a solar elongation angle meeting X-ray observing requirements, $\psi_\odot \geqslant \psi_\odot^{\min}$, where $\psi_\odot^{\min} = 70°$ for XMM-Newton. The smallest heliocentric distance allowed by this constraint is denoted $R^* = 0.943$ au. At this time, the distance between Earth and 1I/'Oumuamua was $\Delta_e^* = 0.276$ au.

$V = 16.6$ at 26 days after perihelion, when 2I/Borisov's distances were $R = 2.1$ au and $\Delta_e = 1.9$ au.

In the following, $Q_{\rm gas}$ denotes the total outgassing rate across all neutral volatiles. In certain instances, a dominant species $X$ was determined, in which case its outgassing rate is denoted $Q(X)$. Our predictions for $L_X$ neglect subtle dependencies on properties of the SW and coma. In the optically thick regime, all SW minor ions will undergo CX. However, the X-ray lines emitted depend on the neutral composition (Mullen et al. 2016). Also, CX cross sections depend strongly on the SW velocity (Beiersdorfer et al. 2001; Kharchenko & Dalgarno 2001; Bodewits et al. 2007).

### 3.1. Analytic Predictions for 2I/Borisov

For 2I/Borisov, we adopt the measured production rate $Q(\mathrm{CO}) = 1.07 \times 10^{27}$ s$^{-1}$ at $R = 2.07$ au (Bodewits et al. 2020). We note that Equation (B8) would predict $Q_{\rm gas} = 5.9 \times 10^{26}$ s$^{-1}$ near perihelion, and modifying the scaling relation to take into account a CO composition (i.e., an $\mathcal{H}$ appropriate for CO ice) yields $Q_{\rm gas} = 4.0 \times 10^{27}$ s$^{-1}$, which are both within an order of magnitude of the observed value. Accounting for the reduced SW density at 2 au, we calculate $L_X = 7.5 \times 10^{11}$ erg s$^{-1}$ (see Table 2). A 900 cm$^2$ effective area (characteristic of EPIC pn) at Earth would detect $6.3 \times 10^{-5}$ counts s$^{-1}$, which would require a considerable 400 ks exposure for a $5\sigma$ detection. Indeed, most previous CX detections in comets have involved much brighter X-ray luminosities $L_X > 10^{14}$ erg s$^{-1}$ (Lisse et al. 1999, 2004).

Since there are observations of 2I/Borisov at multiple points along its trajectory, we may perform a more detailed comparison between our model and the measurements of outgassing over time. We plot the observed time evolution of $Q(\mathrm{H_2O})$ and $Q(\mathrm{CO})$ in Figure 4 with our production rate model (Equation (B8)). Our model, which was calibrated to observations of C/1996 B2 (Hyakutake), predicts water production rates within a factor of a few of those observed. The discrepancies may be due to composition inhomogeneities in the nucleus and/or the sporadic nature of the outgassing. On the other hand, our high model values show that 2I/Borisov could not be made of pure CO, but is more in line with the ∼10%–20% versus water maximal abundances of CO found in solar system comets (Bockelée-Morvan & Biver 2017).

### 3.2. Analytic Predictions for 1I/'Oumuamua

As a baseline estimate for 1I/'Oumuamua, we assume a bulk composition of CO, which is energetically compatible with the nongravitational acceleration and revised Spitzer limits on the production rate, given the low activity state outbound at 2 au (Trilling et al. 2018; Seligman et al. 2021). Equation (B8) with $\mathcal{H}$ corresponding to a CO composition suggests $Q_{\rm gas} = 2.8 \times 10^{28}$ s$^{-1}$ at perihelion (the leftmost marker in Figure 2) and $Q_{\rm gas} = 4.4 \times 10^{26}$ s$^{-1}$ at 2 au, in agreement with the Seligman et al. (2021) estimate, as expected.

With the X-ray flux received at Earth depending strongly on the target's distance from the Sun, 1I/'Oumuamua would have only become accessible to XMM-Newton at its minimum observable heliocentric distance $R = 0.943$ au. This geometry is depicted in Figure 3. It would have been prudent to observe 1I/'Oumuamua in X-ray at this time, which roughly corresponded with 1I/'Oumuamua's closest approach to Earth.

At $R = 0.943$ au and $\Delta_e = 0.276$ au, we estimate $Q_{\rm gas} = 2.0 \times 10^{27}$ s$^{-1}$, $L_X = 1.2 \times 10^{13}$ erg s$^{-1}$, and a flux at Earth of $F_X = 5.4 \times 10^{-14}$ erg s$^{-1}$ cm$^{-2}$. Assuming an $N_2$ (Desch & Jackson 2021) or $H_2$ (Seligman & Laughlin 2020) composition yields even higher $F_X$, as reported in Table 2. For any of these three highly volatile compositions, a signal would have been unambiguously detected in a <1 ks X-ray follow-up exposure, producing a unique, easily obtained, positive outgassing detection.

### 3.3. Observations of CX with Comets

Detections of CX from solar system comets help to gauge the conditions under which we may detect CX from ISOs. The detection of X-rays from C/1996 B2 (Hyakutake; Lisse et al. 1996) prompted Dennerl et al. (1997) to search archival ROSAT data for other instances of CX with comet comae. The confirmed cases include C/1990 Kl (Levy), C/1990 Ni (Tsuchiya-Kiuchi), 45P (Honda-Mrkos-Pajduskova), and C/1991 A2 (Arai). The faintest target was 45P, with $F_X = 1.5 \times 10^{-13}$ erg s$^{-1}$ cm$^{-2}$, which was detected at high confidence by ROSAT with a 191 s exposure.

This comet sample serves as an independent diagnostic for selecting ISOs with detectable CX emission. It is established that a correlation exists between the comet X-ray ($L_X$) and optical ($L_{\rm opt}$) luminosities (e.g., Lisse et al. 1999, 2004). $L_X$ plateaus for the brightest comets, but follows a linear trend for modest luminosities $L_X < 10^{15}$ erg s$^{-1}$, where $L_X \sim 10^{-4} L_{\rm opt}$; however, there is a dependence on the dust-to-gas ratio [D/G] that induces 1–2 dex of scatter. Using the trend presented by Dennerl et al. (1997), we estimate 2I/Borisov's X-ray luminosity as $L_X = 6.1 \times 10^{12}$ erg s$^{-1}$ near perihelion, based on its $V = 16.6$. For 1I/'Oumuamua, at a close approach to Earth and $V = 19.7$, we find $L_X = 2.6 \times 10^9$ erg s$^{-1}$. (Note that

**Table 2**
Estimated X-Ray Luminosity ($L_X$) and Flux ($F_X$) of 2I/Borisov and 1I/'Oumuamua Using Our Model

| Object | Method | $R$ (au) | $Q_{gas}$ ($s^{-1}$) | $L_X$ (ergs $s^{-1}$) | $F_X$ (ergs $s^{-1}$ $cm^{-2}$) |
|---|---|---|---|---|---|
| 2I/Borisov | Measured $Q$(CO) and modeled CX emission. | 2 | $1.07 \times 10^{27}$ | $7.5 \times 10^{11}$ | $6.2 \times 10^{-17}$ |
| 2I/Borisov | Empirical relationship between $L_{opt}$ and $L_X$. | 2 | … | $6.1 \times 10^{12}$ | $6.0 \times 10^{-16}$ |
| 1I/'Oumuamua | Modeled $Q$(CO) and CX emission. | 0.943 | $2.0 \times 10^{27}$ | $1.2 \times 10^{13}$ | $5.4 \times 10^{-14}$ |
| 1I/'Oumuamua | Modeled $Q$(CO) and CX emission at $r_{peri}$. | 0.25 | $2.8 \times 10^{28}$ | $3.3 \times 10^{16}$ | $7.7 \times 10^{-12}$ |
| 1I/'Oumuamua | Modeled $Q(N_2)$ and CX emission. | 0.943 | $1.3 \times 10^{28}$ | $4.7 \times 10^{14}$ | $2.2 \times 10^{-12}$ |
| 1I/'Oumuamua | Modeled $Q(H_2)$ and CX emission. | 0.943 | $1.5 \times 10^{28}$ | $6.9 \times 10^{14}$ | $3.2 \times 10^{-12}$ |
| 1I/'Oumuamua | Empirical relationship between $L_{opt}$ and $L_X$. | 0.943 | … | $2.6 \times 10^{9}$ | $3.6 \times 10^{-17}$ |

**Notes.** For 1I/'Oumuamua, the quoted outgassing rates ($Q_{gas}$) depend on the object's assumed bulk composition and heliocentric ($R$) and geocentric ($\Delta_e$) distances. 1I/'Oumuamua's pericenter was $R = r_{peri} = 0.25$ au; however, the solar elongation constraint for XMM-Newton was first satisfied at $R = 0.943$ au. For 2I/Borisov, we quote values based on our CX emission model, but adopted the measured $Q$(CO) (Bodewits et al. 2020). For both objects, we also estimate $L_X$ from an empirically derived relationship with $L_{opt}$.

this estimate likely underestimates the X-ray emission from 1I/'Oumuamua and serves only as a foil to other estimates presented in this section.)

It is worth mentioning that dusty comae (e.g., C/Hale-Bopp 1995 O1 or 17P/Holmes; Lisse et al. 1997, 2013) may destroy SW ions without concomitant CX X-ray production (Dennerl et al. 1997; Lisse et al. 2004). This effect may prove an obstacle to X-ray observations of dusty ISOs. However, the typical dust content of ISOs is unclear. Jewitt et al. (2017) and Meech et al. (2017) placed stringent upper bounds on 1I/'Oumuamua's dust production rate, at $2 \times 10^{-4}$ kg $s^{-1}$ and $1.7 \times 10^{-3}$ kg $s^{-1}$, respectively. Estimates of 2I/Borisov's rate reach as high as 35 kg $s^{-1}$ (Kim et al. 2020).

## 4. Future ISO CX X-Ray Expectations

For the prospects of detecting CX X-ray emission with a future ISO, it is important to establish: (1) a set of criteria that provides high odds of detecting CX X-ray emission; and (2) an estimated fraction of the ISOs discovered that will exhibit a detectable X-ray flux. To accomplish these goals, we conduct a Monte Carlo analysis assuming Rubin Observatory sky parameters (as the largest and deepest continual all-sky survey of the next decade; e.g., Li et al. 2022), which incorporates baseline predictions for the distribution of perihelia and the geocentric distances of ISO trajectories, as well as their size distribution and possible compositions.

### 4.1. Trajectories

Our Monte Carlo analysis involves randomly drawing orbital configurations for ISOs from previous population synthesis studies. We predict the X-ray flux at the minimum heliocentric distance that satisfies the solar elongation angle constraint of XMM-Newton. This alignment occurs at time $t^*$, defined as

$$t^* \equiv \underset{t}{\text{argmin}} \quad \|\boldsymbol{R}(t)\| \quad \text{s.t.} \quad \cos^{-1}\left(-\frac{(\boldsymbol{R}(t) - \boldsymbol{R}'(t)) \cdot \boldsymbol{R}'(t)}{\|\boldsymbol{R}(t) - \boldsymbol{R}'(t)\|\|\boldsymbol{R}'(t)\|}\right) \geqslant \psi_{\odot}^{\min}, \quad (7)$$

where $\boldsymbol{R}$ and $\boldsymbol{R}'$ are vectors representing the positions of the ISO and Earth, respectively, with the Sun at the origin. The ISO's hyperbolic trajectory may be expressed in a Cartesian coordinate system, where $\boldsymbol{R} = \{R_1, R_2, 0\}$:

$$R_2 = \pm\sqrt{e^2 - 1} \times \sqrt{(R_1 + eq/(e-1))^2 - (q/(e-1))^2}, \quad (8)$$

with the eccentricity $e > 1$ and perihelion $r_{peri}$ sampled from the distributions provided by Hoover et al. (2022). Their study coupled dynamical simulations with the local stellar velocity dispersion to constrain the population of 1I/'Oumuamua-like ISOs that the Rubin Observatory will find. They computed the probability density of perihelia, indicating that 10%, 25%, and 50% of the detected ISOs will attain $r_{peri} \leqslant 0.35$, 0.54, and 0.83 au, respectively. Under this distribution, it is clear that 2I/Borisov had an unlikely large perihelion at 2 au (and was anomalous with respect to other orbital parameters, such as the distance from the solar apex at encounter and eccentricity). By contrast, 1I/'Oumuamua's perihelion distance of 0.25 au was unexpectedly small.

Next, we sample Earth's position as a unit vector with azimuthal and polar angles jointly distributed according to $p(\theta, \phi) = \sin\phi/4\pi$ and scaled by 1 au. In reality, the orientation of the ISO's trajectory with respect to the ecliptic is determined by the inbound velocity vector and impact parameter. Stellar kinematics are a good proxy for the galactic distribution of ISOs; however, the typical ages of ISOs are poorly constrained at a population level. We assume the above distribution of $(\theta, \phi)$ for our order-of-magnitude calculations. The distances $R^* = \|\boldsymbol{R}(t^*)\|$ and $\Delta_e^* = \|\boldsymbol{R}(t^*) - \boldsymbol{R}'(t^*)\|$ are solved for numerically by fixing Earth's position and assuming $\psi_{\odot}^{\min} = 70°$. These distances are shown in Figure 3, with 1I/'Oumuamua's trajectory as an example. In cases where the entirety of the ISO's orbit lies within the solar avoidance zone, the Monte Carlo X-ray flux is immediately set to zero.

We neglect the hyperbolic velocity $v_\infty$ in our analysis, since the vast majority of ISOs accessible to the Rubin Observatory will have $v_\infty \leqslant 40$ km $s^{-1}$. Larger velocities, however, would augment the SW ion collision rate by a factor of 10% or greater. It is prudent to conduct X-ray observations of such ISOs during the inbound portions of their trajectories.

### 4.2. Bulk Properties

The composition of a neutral medium does not strongly affect the X-ray power density from CX in the optically thick regime. However, the coma's density profile depends on the neutral production rate, which in turn depends on the volatility

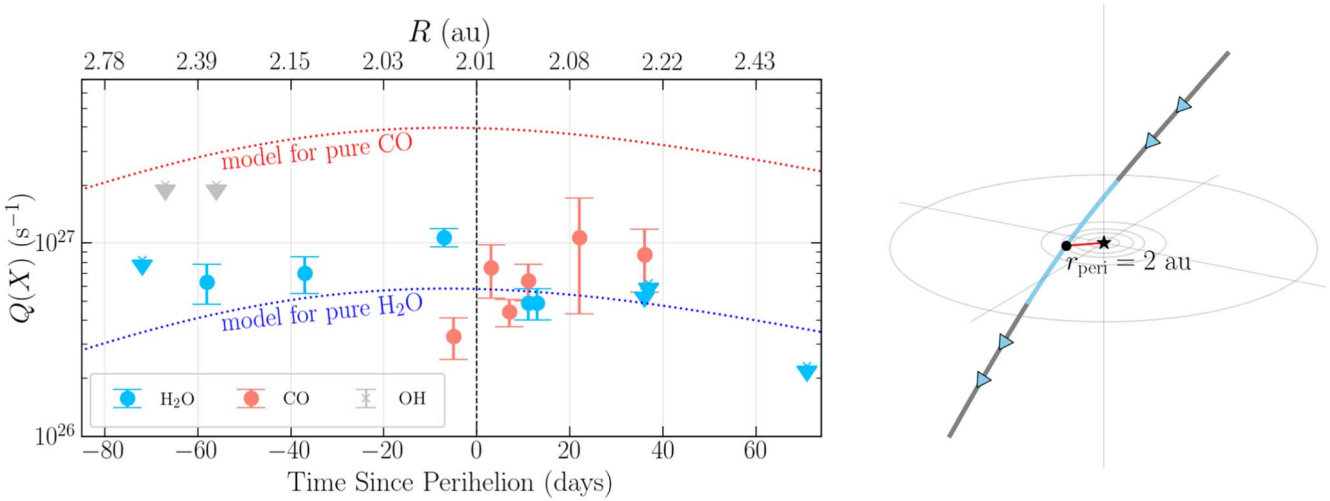


**Figure 4.** Time evolution of the production rates for 2I/Borisov near perihelion (for CO, $H_2O$, and OH). Figure adapted from Seligman et al. (2022). The references for data are provided in their Table 2. The measurements demonstrate that the CO production was substantially greater than the $H_2O$ production after perihelion—the only time when both species were observed contemporaneously. Our production rate model (Equation (B8)) is plotted as dashed lines, holding 2I/Borisov's radius as a constant $a = 0.3$ km and adopting an appropriate $\mathcal{H}$ for $H_2O$ and CO. We obtained 2I/Borisov's heliocentric distance with a `rebound` (Rein & Liu 2012) simulation using the Mercurius integrator (Rein et al. 2019). For reference, the trajectory of 2I/Borisov through the solar system is shown in the right panel, with perihelion marked. The solid blue portion corresponds to the time span plotted in the left panel.

of the surface material in the nucleus of an ISO. While Equation (B8) estimates the neutral production for bulk compositions similar to C/1996 B2 (Hyakutake), it is straightforward to account for alternative materials. The flux of the molecules ejected from a unit surface area patch of the object (in units of $s^{-1}$ $cm^{-2}$) is (e.g., Seligman et al. 2022)

$$\mathcal{N} = \frac{(1-p)I(t) - \epsilon\sigma T_{\rm Sub}^4}{\Delta H/\mathcal{N}_A + \gamma k_B T_{\rm Sub}}. \tag{9}$$

In the above, $p$ is the albedo, $I(t)$ is the time-dependent solar irradiance, and $\epsilon$ is the surface emissivity. Besides $I(t)$ and physical constants, each parameter in the above equation is material-dependent. In practice, graybody emission from the minor body is negligible and the incident radiation term dominates. Using the definition in Equation (B9), exchanging $I(t)$ for the incident solar flux and integrating Equation (9) over the illuminated surface area ($\Sigma_I$) yields

$$Q_{\rm gas} = (1-p)\iint_S \left(\frac{L_\odot}{4\pi R^2 \mathcal{H}}\right) d\Sigma_I. \tag{10}$$

The albedo is unconstrained, but is likely of the order $p \sim 0.1$ for most minor bodies in the solar system. The average projected surface area over all viewing angles is one-fourth times the total surface area for any convex object (Meltzer 1949), so $\Sigma_I \simeq \Sigma/4$, where $\Sigma$ is the total surface area of the object. For a sphere, $\Sigma_I = \pi a^2$, where $a$ is the radius as defined earlier in this paper. Therefore, Equation (10) has the same functional form as Equation (B8).

Hoover et al. (2022) noted that the size distribution of ISOs could enhance the Rubin Observatory's yield and estimated the detection rates for a range of absolute magnitudes (see their Table 2). Many minor body populations adhere to a power-law size distribution,

$$n(>a) = ka^{-\beta}, \tag{11}$$

for some power-law index $\beta$ and normalization constant $k$. Do et al. (2018) note that $\beta > 3$ for ISOs, or else the mass would diverge at large radii. In a collisionally evolved system, $\beta = 2.5$ (Dohnanyi 1969). However, solar system comets have a more complex collisional history, with a power-law index that depends on the size regime. For example, $\beta = 1.45$ in the 1–10 km range and $\beta = 1.91$ in the 2–5 km subset (Meech et al. 2004). For main-belt asteroids, $\beta = 1.0$–$1.4$ for subkilometer diameters (depending on the location within the belt) and $\beta = 1.8$ for larger objects (Yoshida et al. 2003). The distribution for ISOs may be shallow in the case where they are ejected from their respective systems before attaining collisional equilibrium. Also, the bulk of the ISOs may be well described by a single value of $\beta$, but the frequency will necessarily drop off for the largest and smallest objects, due to physical limitations. We incorporate the uncertainty surrounding $\beta$ into our analysis by drawing it randomly from a uniform distribution: $\beta \sim \mathcal{U}(1.0, 2.0)$. As more ISOs are detected, it will be important to reconsider their size distribution.

### 4.3. X-Ray Flux

We further restrict the number of free parameters by assuming the Rubin Observatory will detect 1.5 ISOs per year, the average of the optimistic and conservative rates presented by Hoover et al. (2022). The remaining free parameters are $a$, $R$, and composition. We randomly draw a nuclear radius $a$ by first drawing a value for $\beta$ and subsequently sampling Equation (11). We truncate the distribution at $a_{\rm min} = 25$ m and $a_{\rm max} = 10$ km, which prohibits ISOs larger than most solar system comets and also guarantees they are large enough to realistically be detected by the Rubin Observatory (an object with one-fourth the radius of 1I/'Oumuamua and the same albedo will have $V = 24$ at the same $q = 0.25$ au). The new cumulative probability distribution is

$$n(>a) = \frac{(a^{-\beta} - a_{\rm max}^{-\beta})}{(a_{\rm min}^{-\beta} - a_{\rm max}^{-\beta})}. \tag{12}$$

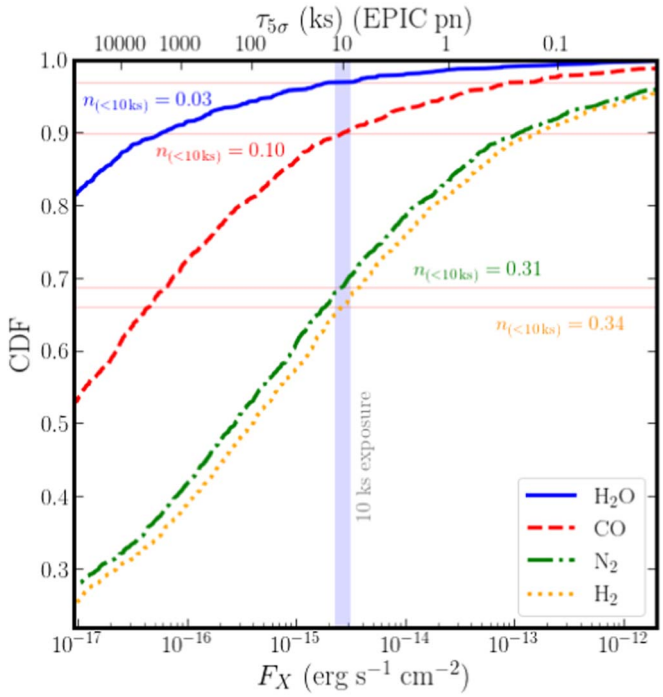


**Figure 5.** Cumulative distribution functions of X-ray flux ($F_X$) for ISOs detected by the Rubin Observatory. Equivalently, the fractions of ISOs detected by the Rubin Observatory that will exhibit a given X-ray flux or less. Four distributions are depicted, each corresponding to an ISO population comprised of a different pure volatile: $H_2O$ (blue), CO (red), $N_2$ (green), and $H_2$ (orange). On the top $x$-axis, $F_X$ is converted into an exposure duration ($\tau_{5\sigma}$) that would yield a $5\sigma$ detection with the XMM-Newton EPIC pn. The vertical blue line delineates $F_X \simeq 2.7 \times 10^{-15}$ erg s$^{-1}$ cm$^{-2}$—a signal that would be detected at $5\sigma$ confidence with a 10 ks exposure. For example, about 10% of CO-dominated ISOs detected by the Rubin Observatory will exhibit this X-ray flux or greater.

The minimum allowed heliocentric distance $R = R^*$ is determined per Equation (7), and the neutral production is calculated using Equation (B8) for four representative pure compositions: $H_2$, $N_2$, CO, and $H_2O$. We make an important modification, however, by drawing the heliocentric distance scaling exponent from a random uniform distribution $x \sim \mathcal{U}(-4.33, -1.82)$ as opposed to a fixed $x = -2$, per Combi et al. (2019). The CX flux is then calculated using Equation (B3) and an optically thick cross section given by Equation (B6) and the correction factor $\kappa$.

Figure 5 summarizes our results and demonstrates the viability of using X-rays as a diagnostic probe of ISOs across different compositional assumptions. As discussed earlier, composition has a profound effect on the extent of the outgassed coma and the expected X-ray flux. In the most conservative scenario, that ISOs are predominantly composed of water ice, then about 3% found by the Rubin Observatory will exhibit $F_X \gtrsim 2.7 \times 10^{-15}$ erg s$^{-1}$ cm$^{-2}$, which can be robustly detected by a 10 ks exposure (i.e., $\tau_{5\sigma} = 10$ ks corresponds to a $5\sigma$ detection; about 6% are accessible with a $\tau_{5\sigma} = 100$ ks exposure). Another 90% of $H_2O$-dominated ISOs will exhibit undetectable levels of CX emission (i.e., $\tau_{5\sigma} > 1000$ ks). If CO is the dominant constituent of ISOs, then about 10% will emit X-rays detectable with a 10 ks exposure. The detectability fraction is even higher for the most volatile compositions, reaching 31% for $N_2$ ice and 34% for $H_2$ ice. With a longer 100 ksec exposure, these fractions reach 19%, 47%, and 50% for CO, $N_2$, and $H_2$, respectively.

These statistics suggest that the Rubin Observatory will discover new ISOs amenable to X-ray spectroscopic characterization. If the survey finds 15 2I/Borisov analogs (i.e., CO-dominated interstellar comets) over a 10 yr campaign, then approximately one to two of them will be accessible with a 10 ks EPIC pn exposure. The Rubin Observatory will probably detect one such ISO in its first 5 yr of operation. The approach is similarly effective for 1I/'Oumuamua analogs. X-ray emission should be detectable for about one-third of $N_2$-dominated and $H_2$-dominated ISOs. On the other hand, consistent nondetections of CX emission will point to an alternative, refractory composition. For objects that exhibit nongravitational acceleration, a lack of X-rays may also indicate an alternative mechanism that provides the required force (e.g., radiation pressure).

## 5. Conclusions

In this paper, we propose X-ray spectroscopy as a means of detecting outgassed comae and revealing highly volatile compositions of ISOs, a new class of astrophysical phenomena. The neutral gas comae of ISOs should undergo CX with SW ions in the same manner as has been widely observed with solar system comets. We suggest a tiered list of scientific goals that are realistically achievable by existing and concept X-ray missions, sorted by feasibility:

1. Photometric detection of CX (i.e., at $\geqslant 5\sigma$ significance) in order to detect an outgassed coma. Modest exposure times of order 10 ks may reveal a statistically significant X-ray flux originating from an ISO, particularly when observed at heliocentric distances $R \lesssim 1$ au. The viable parameter space is depicted in Figure 2 for the pn on board XMM-Newton. Confidently detecting X-ray emission over a bandpass of 0.5–0.7 keV would immediately reveal the existence of a coma undergoing CX with SW ions. X-ray observations of 1I/'Oumuamua near its close approach to Earth would have either confirmed the presence of a coma or placed an upper bound on the production rate to a point that another mechanism would be necessary to explain the anomalous acceleration.
2. Joint constraints on $a$ and $Q_{\mathrm{gas}}$ in order to infer an ISO's volatile content. Once an ISO's ephemeris is determined, the X-ray flux is degenerate with $a$ and $\mathcal{H}$. By assuming a range of plausible albedos, one can constrain $a$ from an optical lightcurve (e.g., Mashchenko 2019). The radius is also constrained by the energetics of nongravitational acceleration. For example, Seligman & Laughlin (2020) suggested various ices ($H_2$, Ne, $N_2$, Ar, $O_2$, Kr, Xe, $CO_2$, and $H_2O$) that could be compatible with 1I/'Oumuamua's outbound acceleration. For a subset of these species ($N_2$, $H_2$, CO, Ne, plus $CH_4$), Jackson & Desch (2021) showed the relationship between nongravitational acceleration, albedo, and mean spherical radius. Across these different species, the allowable range for $a$ lies between 20 and 25 m for albedo $p > 0.6$. However, their respective sublimation energies ($\mathcal{H}$) vary by a factor of 10, which, according to our model, implies that $\mathcal{A}$ varies by a factor of 100. This interaction area is probed by the X-ray flux from CX. If the nuclear radius of an ISO can be constrained within a factor of order unity, then an

anomalously high $F_X$ would immediately reveal an exotic, highly volatile composition, due to the inverse proportionality between $Q_{gas}$ and $\mathcal{H}$. We reiterate that a nondetection in X-ray would favor low-volatility ices (e.g., $H_2O$ or $CO_2$) or an alternative acceleration mechanism.

3. Measuring line strength ratios toward robustly determining the coma composition. Mullen et al. (2017) demonstrated that relative CX emission line strengths (including strong transitions from CV, CVI, and OVII) depend on the neutral target medium. Specifically, $N_2$, $H_2O$, O, OH, CO, and $CO_2$ targets were considered in their study. A high-fidelity X-ray spectrum may be achievable by existing facilities for the brightest ISOs. However, this method is most amenable to next-generation X-ray telescopes that feature both large effective areas and high spectral resolution. A detailed study of this approach, and its feasibility with X-ray concept missions, would be scientifically useful.

Baseline estimates of the Rubin Observatory's yield suggest around 15 new ISOs over a 10 yr campaign. If these objects are predominantly composed of CO, about one or two will exhibit detectable levels of X-ray flux. In the case that most ISOs are comprised of $H_2$ ice, CX will be observable for about five of them. Efforts to understand this mysterious population benefit from broadband spectroscopy—infrared, optical, and UV observations provide complementary insights into physical and chemical properties of the nucleus and coma. As X-ray observations of CX with comets has been an active area of study, similar efforts directed toward ISOs will at the very least reaffirm findings made at other wavelengths, and potentially discern the true compositions of these minor bodies.

## Acknowledgments

We thank the two referees of this manuscript for their constructive comments, which significantly improved the presentation of the paper. We extend particular thanks to Carey Lisse for a number of detailed and insightful recommendations which led to a much stronger final version. We also thank Greg Laughlin for his review of the manuscript and for constructive discussions. D.Z.S. acknowledges financial support from National Science Foundation grant No. AST-2107796, NASA grant No. 80NSSC19K0444, and NASA Contract NNX17AL71A from the NASA Goddard Spaceflight Center. D.Z.S. is supported by an NSF Astronomy and Astrophysics Postdoctoral Fellowship under award AST-2202135. This research award is partially funded by a generous gift of Charles Simonyi to the NSF Division of Astronomical Sciences. The award is made in recognition of significant contributions to Rubin Observatory's Legacy Survey of Space and Time.

## Appendix A
## Review of SW CX

Since the discovery of strong X-ray emission from a cool cometary source, C/Hyakutake 1996 B2, by Lisse et al. (1996), SW CX has gained considerable traction for its ability to explain X-ray emission from objects within the solar system. CX models have successfully explained observed X-rays from the volatile comae of solar system comets (Cravens 1997; Wegmann et al. 1998), as well as emission originating from Earth (Wargelin et al. 2004; Fujimoto et al. 2007), Mars (Kallio et al. 1997; Dennerl 2002), Venus (Dennerl et al. 2002), and Jupiter (Metzger et al. 1983; Cravens et al. 2003).

In order to produce X-ray emission, heavy ions from the SW interact with cool atomic and molecular gas surrounding the object. This process also produces a source of X-ray emission from star-forming galaxies such as M82 (e.g., Liu et al. 2012; Zhang et al. 2014). In such a galaxy, CX occurs at the interface between hot and cool interstellar gases, likely responsible for the enhanced forbidden transitions of K$\alpha$ triplet emissions from He-like ions and high-order transitions in Lyman series of H-like ions (Zhang et al. 2014). There has also been tentative detection of CX in galaxy clusters (Gu et al. 2018).

The general CX reaction is

$$A^{q+} + N \rightarrow (A^*)^{(q-1)+} + N^+, \tag{A1}$$

where the ion $A^{q+}$ gains an electron from the neutral species N (atomic or molecular, often H, $H_2$, and He). The integer q denotes the initial ionization state of the species A. The electron is in an excited state, denoted by the superscript $^*$. As it cascades to the ground state, the electron emits X-ray and UV photons. Implicit in this equation are the initial and final-state quantum numbers ($n$, $l$, and $m$) of the transferred electron. The most probable final-state principal quantum number $n$ is given by Equation (2.6) of Janev & Winter (1985), which is an approximation that is generally applied while modeling this process (Smith et al. 2012).

The CX interaction cross section ($\sigma_{sq}$) for a given species (denoted by the subscript s) and charge (denoted by the subscript q) was modeled by Wegmann et al. (1998) and is given by

$$\sigma_{s\,q} = \left( \frac{q - 1}{q^2/2n^2 - |I_{p,\,s}/27.2\ \mathrm{eV}|} \right)^2 \times 0.88 \times 10^{-16}\ (\mathrm{cm}^2). \tag{A2}$$

The variables q and $I_{p,\,s}$ in Equation (A2) correspond to the dimensionless integer charge of the ion and ionization potential (measured in eV) of the target species, respectively.

For comets, the SW typically interacts with volatile coma particles. Some of the most common target species outgassed by solar system comets are water and its constituents (O, OH, and H; Cochran et al. 2015; Biver & Bockelée-Morvan 2016; Bockelée-Morvan & Biver 2017). All of these species have similar ionization energies ~13 eV (Wegmann et al. 1998). CX cross sections are $\sim 10^{-15}$–$10^{-14}$ cm$^2$ for heavy SW ions such as O VIII, O VII, C VII, C VI, NVII, Ne IX, Si X, and Fe XII. That is, CX occurs when these ions come within ~1 nm of the neutral targets. The energy difference between the captured electron's initial (excited) state and ground state ($E_{excit}$) can reach several hundreds of eV. Therefore, these transitions provide significant contributions to EUV and X-ray radiation. CX emission from cometary comae has rich observational and theoretical backing, as reviewed by Bodewits et al. (2012) and Dennerl et al. (2012).

Our main concern is CX between the SW and the outgassed species within an ISO's coma. Assuming that a given SW ion undergoes CX once during its passage through the neutral medium, the X-ray power density $P_{sj}$ for transition (j) at a given

position $\boldsymbol{r}$ is (Cravens 1997, 2000; Cravens et al. 2009)

$$P_{\rm sj}(\boldsymbol{r}) = \Phi_{\rm sq}(\boldsymbol{r})\sigma_{\rm sq}\, b_{\rm sqj}\, n_{\rm n}(\boldsymbol{r})\Delta E_{\rm sqj}, \tag{A3}$$

which has units of eV cm$^{-3}$ s$^{-1}$. Here $\Phi_{\rm sq}$ denotes the SW flux of a given ion, $\sigma_{\rm sq}$ is the CX cross section (Equation (A2)), $b_{\rm sqj}$ is the spectral cascading probability for transition (j), which releases a photon of energy $\Delta E_{\rm sqj}$, and $n_{\rm n}$ is the number density of neutral species. The SW flux may be written as $\Phi_{\rm sq} = f_{\rm sq} n_{\rm SW} u_{\rm SW}$, where $n_{\rm SW}$ and $u_{\rm SW}$ correspond to the SW proton number density and velocity, respectively. The SW fraction of a given species/charge is $f_{\rm sq}$. These quantities are functions of positions in space. For example, the unshocked SW has a typical speed of ~400 km s$^{-1}$ and density of ~0.4 cm$^{-3}$ at 5 au (Cravens et al. 2003). The density $n_{\rm SW}$ falls off as the square of the distance from the host star (Cravens 2000). While the SW flux varies over time, the fraction of heavy ions to protons in the SW remains fairly consistent at $f \approx 10^{-3}$. The intensity is obtained by integrating Equation (A3) over a given path length (i.e., performing a line integral).

## Appendix B
## CX with Outgassed Comae

Our prescription for CX emission is calibrated to observations of C/1996 B2 (Hyakutake) and early models that described its X-ray luminosity. Wegmann et al. (1998) calculated the total X-ray emissivity by summing over all SW ions in Equation (A3). They adopted parameter values of $\sigma_{\rm sq} = 3 \times 10^{-15}$ cm$^2$, $f_{\rm O} = 0.0005$, and 1100 eV emitted per oxygen ion in the SW, based on summing the CX excited-state energies of all ions and weighting them according to their relative abundance fraction. Further, they assumed an "effectivity" of 0.4, which replaces the $b_{\rm sqj}$ terms. The power density is approximately

$$P_{\rm X}(\boldsymbol{r}') = 4 \times 10^{-20} n_{\rm SW} n_{\rm n}(\boldsymbol{r}') \text{ erg cm}^3 \text{ s}^{-1}, \tag{B1}$$

where the density of the neutrals at distance $\boldsymbol{r}'$ from the comet's nucleus follows

$$n_{\rm n}(\boldsymbol{r}') = \left( \frac{Q_{\rm gas}}{4\pi v |\boldsymbol{r}'|^2} \right) e^{-|\boldsymbol{r}'|/\lambda}, \tag{B2}$$

for a total neutral production rate $Q_{\rm gas}$, outflow velocity $v$, and photodestruction length scale $\lambda$. Wegmann et al. (1998) adopted $Q_{\rm gas} = 1.5 \times 10^{29}$ s$^{-1}$ and $n_{\rm SW} = 7$ cm$^{-3}$. By neglecting photodestruction, which Cravens (1997) deemed negligible within $5 \times 10^5$ km, and adopting a nominal $v = 1$ km s$^{-1}$, integration over a sphere of beam radius 135,000 km yields $L_{\rm X} \sim 6 \times 10^{15}$ erg s$^{-1}$, comparable to the measured luminosity and other estimates in the literature. As follows, we determine expectations for CX emission from the comae of other minor bodies.

### *B.1. Luminosity from the Optically Thick Coma*

CX produces a surface luminosity, $4\pi I$ (Cravens et al. 2003), given by the equation

$$4\pi I = n_{\rm SW}\, u_{\rm SW}\, f\, N\, \Delta E. \tag{B3}$$

Each ion contributes, on average, $N$ photons of typical energy $\Delta E$, and the SW minor ion fraction is given by $f$. The total luminosity is obtained by integrating Equation (B3) over the effective surface area. Our baseline model assumes that this area is the region where the coma is optically thick to CX. That is, it satisfies the criterion

$$\int_S \left( \sigma_{\rm sq} n_{\rm n}(\boldsymbol{r}') \right) ds > 1 \tag{B4}$$

for a linear projected path $S$ of the SW through the coma, where $\boldsymbol{r}'$ is the distance from the cometary nucleus as in Equation (B2). As long as the coma neutral column is large enough that the SW is fully depleted of all highly stripped minor ions, the individual transition probabilities are not important. For simplicity, we also fix the cross section at $\sigma_{\rm sq} = 3 \times 10^{-15}$ cm$^2$. This value is consistent with expectations from the ionization potentials of $H_2$ ($I_{p,s} \approx 15.4$ eV) and $N_2$ ($I_{p,s} \approx 15.6$ eV). Considering these compositions and those more typical of comets, we find $2 \times 10^{-15}$ cm$^2$ $\leqslant \sigma_{\rm sq} \leqslant 13 \times 10^{-15}$ cm$^2$ for ion charges $+5 \leqslant q \leqslant +7$. We assume that the coma is approximately spherical and follows a neutral density profile given by Equation (B2). We define the impact parameter, $b$, as the minimum distance between the path $S$ and the nucleus. Also, let $R$ be the distance between the Sun and the nucleus and assume that $R \gg b$. We parameterize the path $S$ as a function of $\boldsymbol{r}'$. We define the dimensionless parameter $x \equiv |\boldsymbol{r}'|/b$ and a coefficient $K \equiv \sigma_{\rm sq} Q_{\rm gas}/4\pi w$. By substituting Equation (B2) into Equation (B4) with these new parameters, the optically thick transition occurs where

$$\frac{2K}{b} \int_1^\infty \frac{1}{x\sqrt{x^2 - 1}} e^{-bx/\lambda} dx = 1, \tag{B5}$$

or, equivalently, where

$$\frac{2K}{b} \int_0^{\pi/2} e^{-b \sec\theta/\lambda} d\theta = 1. \tag{B6}$$

Equation (B6) is equivalent to a function $b = b(\sigma_{\rm sq}, w, \lambda, Q_{\rm gas})$, which may be evaluated numerically. It returns a distance within which the coma is optically thick to CX. For physically plausible photodestruction scales of $\lambda = 10^8$–$10^{11}$ cm (Combi et al. 2004), a reasonable approximation is that $b \propto Q_{\rm gas}$ in the regime $Q_{\rm gas} < 10^{28}$ s$^{-1}$. Figure 6 shows the validity of this approximation for different assumed $\lambda$. As $\lambda \to \infty$, the function approaches a linear relationship.

Taking C/1996 B2 (Hyakutake) as a nominal example (hence the above assumed $\lambda$ and $Q_{\rm gas}$ values), we find $b \approx$ 10, 000 km, which is in reasonable agreement with the 30,000 km penetration depth estimated by Wegmann et al. (1998). In order to estimate the total X-ray luminosity, we assume $n_{\rm SW} = 7$ cm$^{-3}$ at 1 au, $u_{\rm SW} = 400$ km s$^{-1}$, $f = 0.001$, $N = 1$, and $\Delta E = 550$ eV. The above equations predict $L_{\rm X} = 8.2 \times 10^{14}$ erg s$^{-1}$ from the optically thick region alone. This estimate is about five times less than the total luminosity measured by ROSAT. Using a refined hydrodynamical model, Wegmann et al. (2004) also estimated $L_{\rm X}$ for C/1996 B2 (Hyakutake) during its close approach to Earth. Their measurements were centered around $10^{16}$ erg s$^{-1}$, which is higher than the initial estimate from Lisse et al. (1996). The discrepancy between these literature estimates and our own is probably due to significant emission taking place in optically thin regions of the coma, which is currently unaccounted for in our model for the optically

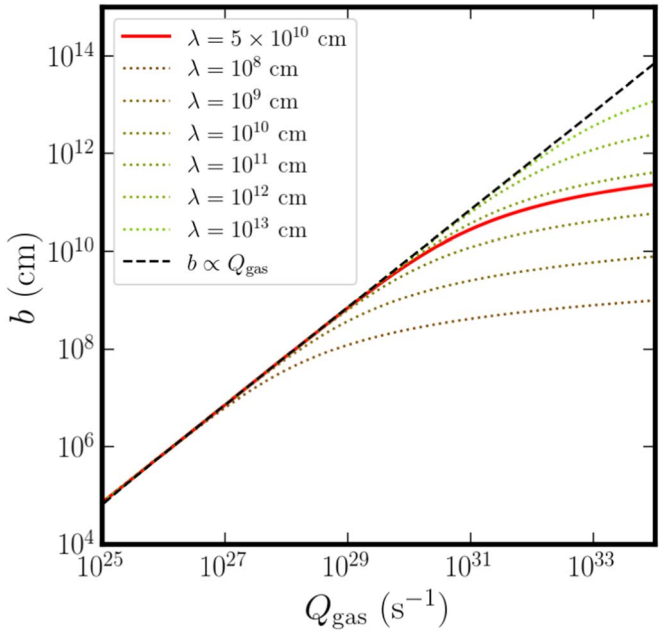


**Figure 6.** The relationship between the outgassing rate $Q_{\rm gas}$ and radius $b$ within which a coma is optically thick to CX. Since $b$ lacks a closed form (Equation (B6)), it is solved for numerically. The function is plotted for several assumptions of the ionization scale $\lambda$. In all cases, $v = 1$ km s$^{-1}$. Our main analysis assumes $\lambda = 5 \times 10^{10}$ cm (the red line). As $\lambda$ increases, the function approaches a linear relationship between $Q_{\rm gas}$ and $b$ (the black dashed line).

thick zone. Therefore, it is useful to calibrate our model and correct for this component per the following.

### *B.2. Extensions to the Analytic Model*

Holding other parameters constant, $b$ scales linearly with $Q_{\rm gas}$ in the regime $Q_{\rm gas} < 10^{30}$ s$^{-1}$ for $\lambda \sim 5 \times 10^{10}$ cm. The CX interaction area in this regime can be approximated by $\pi b^2 \approx \Gamma Q_{\rm gas}^2$, with $\Gamma = 1.5 \times 10^{-40}$ s$^2$ cm$^2$. A similar conclusion was reached by Wegmann et al. (2004), who developed a hydrodynamical model of X-ray emission morphology and applied it to observations of comets. They derived a relationship $L_{\rm X} = CHQ_{\rm gas}^2$, where $H = u_{\rm SW} n_{\rm SW} f N \Delta E$ is the heavy-ion SW flux. By fitting their estimates of $HQ_{\rm gas}^2$ to observed X-ray luminosities of comets, they determined a constant of proportionality $C = 10^{-38}$ s$^2$ cm$^2$. Let $\mathcal{A}$ define an effective, optically thick surface area that would yield a given $L_{\rm X}$. Then the relationship found by Wegmann et al. (2004) is equivalent to $\mathcal{A} = CQ_{\rm gas}^2$. We adopt a correction factor $\kappa \equiv \sqrt{C/\Gamma} \approx 8.1$ that defines a new effective radius:

$$\tilde{b} \equiv \kappa b. \tag{B7}$$

In other words, $\kappa$ is a factor that increases the radius of the CX interaction area from $b$ to $\tilde{b}$, thereby approximately accounting for emission from regions beyond the optically thick zone. Prior observations of CX within cometary comae (e.g., Lisse et al. 1999, 2004) have produced detections of significant X-ray emission extending as little as $\sim 5 \times 10^4$ km (for 2P/Encke 2003) and as far as an apparent limit at $\sim 10^6$ km (for C/1996 B2 (Hyakutake), C/1991 K1 (Levy), and C/1995 O1 (Hale-Bopp)).

We adopt $Q_{\rm gas} \propto a^2 R^{-2}$, where $a$ is the body's radius and $R$ is the instantaneous heliocentric distance. The $R^{-2}$ dependency is the same as that of the incident solar radiation. While physically motivated, this scaling simplifies true cometary activity. Following a long-baseline survey of water outgassed by 61 comets, Combi et al. (2019) found generally steeper scaling: $Q(\mathrm{H_2O}) \propto R^x$, with $-4.33 \leqslant x \leqslant -1.82$, depending on taxonomic class. This finding is incorporated into our expectations for future ISO observations in Section 4.

Our model must also account for the fact that more volatile species will sublimate and outgas at higher rates (potential compositions are discussed further in Section 4). We use the following scaling relation:

$$Q_{\rm gas} = 1.5 \times 10^{29} \times \left(\frac{a}{2.4\ \mathrm{km}}\right)^2 \left(\frac{R}{1\ \mathrm{au}}\right)^{-2} \left(\frac{\mathcal{H}}{9.3 \times 10^{-23}\ \mathrm{kJ}}\right)^{-1} \mathrm{s}^{-1}, \tag{B8}$$

which is calibrated to the nuclear radius of C/1996 B2 (Hyakutake; Lisse et al. 1999) and the production rate adopted by Wegmann et al. (1998). Production rates for OH were measured by Schleicher (1996) and varied from $\log_{10} Q(\mathrm{OH}) = 28.89$ (at $R = 0.94$ au) to $\log_{10} Q(\mathrm{OH}) = 29.17$ (at $R = 1.08$ au). In the above, $\mathcal{H}$ is the total energy input for each coma particle:

$$\mathcal{H} \equiv \Delta H / \mathcal{N}_A + \gamma k T_{\rm Sub}. \tag{B9}$$

The above expression involves the enthalpy of sublimation ($\Delta H$), temperature of sublimation ($T_{\rm Sub}$), and adiabatic index of the escaping vapor ($\gamma$), all of which are material-dependent (Table 1). The quantity $\mathcal{H}$ is the sum of two components: the energy required to sublimate an ice molecule (the first term) and the energy required to heat the molecule to the outflow velocity (the second term). In the case of water, $\mathcal{H}_{\rm H_2O} = 9.3 \times 10^{-23}$ kJ (values for other species are listed in Table 1). Chemical properties also determine the outgassing velocity $v$:

$$v \simeq c_s = \sqrt{\gamma k T_{\rm Sub} / \mu m_{\rm H}}, \tag{B10}$$

for mean molecular weight $\mu$ and sound speed $c_s$. For typical values $v = 0.3$–$1$ km s$^{-1}$, $Q < 10^{30}$ s$^{-1}$, photodestruction timescales $t_{\rm photo} < 10^7$ s, and $\lambda = w t_{\rm photo}$, the optically thick radius does not exceed $10^6$ km under our model. It is limited by the exponential decay term in Equation (B2). We reiterate that only monotomic and homonuclear diatomic species (having zero dipole moment) will be more amenable to CX X-ray characterization than to infrared fluorescence spectroscopy.

The normalization in Equation (B8) is to C/1996 B2 (Hyakutake), and the expression should be considered an order-of-magnitude estimate of $Q_{\rm gas}$ for other objects. Ideally, one may use independent estimates of $Q_{\rm gas}$ obtained either from infrared spectroscopy or a more detailed theoretical model that accounts for the target's composition. For most solar system comets, $Q_{\rm gas} \simeq Q(\mathrm{H_2O}) + Q(\mathrm{CO_2}) + Q(\mathrm{CO})$, which is the sum of the production rates of the most common volatile components in comets (Bockelée-Morvan & Biver 2017). Nevertheless, Equation (B8) enables baseline predictions for new minor bodies and is especially useful for population-level predictions when given distributions for $a$ and perihelion $r_{\rm peri}$. Additionally, we assume that the SW proton number density is

given by

$$n_{\rm SW}(R) = 7\ {\rm cm}^{-3}\left(\frac{R}{1\ {\rm au}}\right)^{-2}, \tag{B11}$$

which is maximized at perihelion when $R = r_{\rm peri}$. Note that flares can enhance the SW ion flux, thus improving the feasibility of CX X-ray observations at larger $R$. For example, a flare nearly doubled the soft X-ray count rate from C/1999 S4 (LINEAR; Lisse et al. 2001).

Combining Equations (B3) and (B7), we arrive at a general model for X-ray luminosity:

$$L_{\rm X} = \pi \tilde{b}^2 n_{\rm SW} u_{\rm SW} f N \Delta E, \tag{B12}$$

which is a function of $\{\sigma_{\rm sq},\ \lambda,\ a,\ r_{\rm peri},\ \mu,\ \Delta H,\ \gamma,\ T_{\rm Sub}\}$, assuming observations take place at perihelion. Also, a nominal $\lambda = 5 \times 10^{10}$ cm is adopted for our analysis. We use this model to predict the luminosity of the CX emission with ISOs in Section 4, and a schematic of the entire CX process with ISOs is shown in Figure 1. It is worth explicitly highlighting our model's dependence on perihelion distance. We have demonstrated an approximately linear relationship between $b$ and $Q_{\rm gas}$, where $Q_{\rm gas} \propto r_{\rm peri}^{-2}$ through its dependence on the solar radiation flux $F_\odot \propto r_{\rm peri}^{-2}$. The CX surface area follows $\mathcal{A} \propto b^2$, and the incident heavy-ion flux follows $n_{\rm SW} \propto r_{\rm peri}^{-2}$. Therefore, $L_{\rm X} \propto r_{\rm peri}^{-6}$: the perihelion of an ISO strongly dictates whether its CX X-ray emission is detectable (similar scaling relationships were explored by Lisse et al. 1999).

## ORCID iDs

Samuel H. C. Cabot https://orcid.org/0000-0001-9749-6150
Q. Daniel Wang https://orcid.org/0000-0002-9279-4041
Darryl Z. Seligman https://orcid.org/0000-0002-0726-6480

## References

Aravind, K., Ganesh, S., Venkataramani, K., et al. 2021, MNRAS, 502, 3491
Bailer-Jones, C. A. L., Farnocchia, D., Meech, K. J., et al. 2018, AJ, 156, 205
Bannister, M. T., Opitom, C., Fitzsimmons, A., et al. 2020, arXiv:2001.11605
Batygin, K., & Laughlin, G. 2008, ApJ, 683, 1207
Beiersdorfer, P., Lisse, C. M., Olson, R. E., Brown, G. V., & Chen, H. 2001, ApJL, 549, L147
Bialy, S., & Loeb, A. 2018, ApJL, 868, L1
Bieler, A., Altwegg, K., Balsiger, H., et al. 2015, Natur, 526, 678
Biver, N., & Bockelée-Morvan, D. 2016, IAUFM, 29A, 228
Biver, N., Dello Russo, N., Opitom, C., & Rubin, M. 2022, arXiv:2207.04800
Bockelée-Morvan, D., & Biver, N. 2017, RSPTA, 375, 20160252
Bockelée-Morvan, D., Crovisier, J., Mumma, M. J., & Weaver, H. A. 2004, in Comets II, ed. M. C. Festou, H. U. Keller, & H. A. Weaver (Tucson, AZ: Univ. Arizona Press), 391
Bodewits, D., Christian, D. J., Carter, J. A., et al. 2012, AN, 333, 335
Bodewits, D., Christian, D. J., Torney, M., et al. 2007, A&A, 469, 1183
Bodewits, D., Noonan, J. W., Feldman, P. D., et al. 2020, NatAs, 4, 867
Bolin, B. T., Lisse, C. M., Kasliwal, M. M., et al. 2020, AJ, 160, 26
Bolin, B. T., Weaver, H. A., Fernandez, Y. R., et al. 2018, ApJL, 852, L2
Cochran, A. L., Levasseur-Regourd, A.-C., Cordiner, M., et al. 2015, SSRv, 197, 9
Combi, M. R., Harris, W. M., & Smyth, W. H. 2004, in Comets II, ed. M. C. Festou, H. U. Keller, & H. A. Weaver (Tuscon, AZ: Univ. Arizona Press), 523
Combi, M. R., Mäkinen, T. T., Bertaux, J. L., Quémerais, E., & Ferron, S. 2019, Icar, 317, 610
Cook, N. V., Ragozzine, D., Granvik, M., & Stephens, D. C. 2016, ApJ, 825, 51
Cordiner, M. A., Milam, S. N., Biver, N., et al. 2020, NatAs, 4, 861
Cravens, T. 2000, AdSpR, 26, 1443
Cravens, T. E. 1997, GeoRL, 24, 105
Cravens, T. E. 2000, ApJL, 532, L153
Cravens, T. E. 2002, Sci, 296, 1042
Cravens, T. E., Robertson, I. P., Snowden, S., et al. 2009, in AIP Conf. Proc. 1156, The Local Bubble and Beyond II, ed. R. K. Smith, S. L. Snowden, & K. D. Kuntz (Melville, NY: AIP), 37
Cravens, T. E., Waite, J. H., Gombosi, T. I., et al. 2003, JGRA, 108, 1465
Crovisier, J., & Encrenaz, T. 1983, A&A, 126, 170
Dello Russo, N., Mumma, M. J., DiSanti, M. A., & Magee-Sauer, K. 2002, JGRE, 107, 5095
Dennerl, K. 2002, A&A, 394, 1119
Dennerl, K., Burwitz, V., Englhauser, J., Lisse, C., & Wolk, S. 2002, A&A, 386, 319
Dennerl, K., Englhauser, J., & Trümper, J. 1997, Sci, 277, 1625
Dennerl, K., Lisse, C. M., Bhardwaj, A., et al. 2012, AN, 333, 324
Desch, S. J., & Jackson, A. P. 2021, JGRE, 126, e06807
Do, A., Tucker, M. A., & Tonry, J. 2018, ApJL, 855, L10
Dohnanyi, J. S. 1969, JGR, 74, 2531
Engelhardt, T., Jedicke, R., Vereš, P., et al. 2017, AJ, 153, 133
Ewing, I., Christian, D. J., Bodewits, D., et al. 2013, ApJ, 763, 66
Flekkøy, E. G., Luu, J., & Toussaint, R. 2019, ApJL, 885, L41
Füglistaler, A., & Pfenniger, D. 2018, A&A, 613, A64
Fujimoto, R., Mitsuda, K., McCammon, D., et al. 2007, PThPS, 169, 71
Gomes, R. S., Morbidelli, A., & Levison, H. F. 2004, Icar, 170, 492
Gu, L., Kaastra, J., & Raassen, A. J. J. 2016, A&A, 588, A52
Gu, L., Mao, J., de Plaa, J., et al. 2018, A&A, 611, A26
Hahn, J. M., & Malhotra, R. 1999, AJ, 117, 3041
Hoover, D. J., Seligman, D. Z., & Payne, M. J. 2022, PSJ, 3, 71
Hsieh, C.-H., Laughlin, G., & Arce, H. G. 2021, ApJ, 917, 20
Jackson, A. P., & Desch, S. J. 2021, JGRE, 126, e06706
Janev, R. K., & Winter, H. 1985, PhR, 117, 265
Jewitt, D., Kim, Y., Mutchler, M., et al. 2020, ApJL, 896, L39
Jewitt, D., & Luu, J. 2019, ApJL, 886, L29
Jewitt, D., Luu, J., Rajagopal, J., et al. 2017, ApJL, 850, L36
Jewitt, D., & Seligman, D. Z. 2023, ARA&A, 61, 197
Kallio, E., Luhmann, J. G., & Barabash, S. 1997, JGRA, 102, 22183
Kareta, T., Andrews, J., Noonan, J. W., et al. 2020, ApJL, 889, L38
Kharchenko, V., & Dalgarno, A. 2001, ApJL, 554, L99
Kim, Y., Jewitt, D., Mutchler, M., et al. 2020, ApJL, 895, L34
Knight, M. M., Protopapa, S., Kelley, M. S. P., et al. 2017, ApJL, 851, L31
Koutroumpa, D. 2012, AN, 333, 341
Krasnopolsky, V. 1997, Icar, 128, 368
Laskar, J. 1989, Natur, 338, 237
Laskar, J., & Gastineau, M. 2009, Natur, 459, 817
Levine, W. G., & Laughlin, G. 2021, ApJ, 912, 3
Levison, H. F., Morbidelli, A., Van Laerhoven, C., Gomes, R., & Tsiganis, K. 2008, Icar, 196, 258
Li, X., Ragosta, F., Clarkson, W. I., & Bianco, F. B. 2022, ApJS, 258, 2
Lin, H. W., Lee, C.-H., Gerdes, D. W., et al. 2020, ApJL, 889, L30
Lisse, C., Christian, D., Dennerl, K., et al. 1999, Icar, 141, 316
Lisse, C. M., Christian, D. J., Dennerl, K., et al. 2001, Sci, 292, 1343
Lisse, C. M., Christian, D. J., Wolk, S. J., et al. 2013, Icar, 222, 752
Lisse, C. M., Cravens, T. E., & Dennerl, K. 2004, in Comets II, ed. M. C. Festou, H. U. Keller, & H. A. Weaver (Tuscon, AZ: Univ. Arizona Press), 631
Lisse, C. M., Dennerl, K., Englhauser, J., et al. 1996, Sci, 274, 205
Lisse, C. M., Fernández, Y. R., A'Hearn, M. F., et al. 1997, EM&P, 78, 251
Lisse, C. M., Fernández, Y. R., Kundu, A., et al. 1999, Icar, 140, 189
Lisse, C. M., Gladstone, G. R., Young, L. A., et al. 2022, PSJ, 3, 112
Liu, J., Wang, Q. D., & Mao, S. 2012, MNRAS, 420, 3389
Luu, J. X., Flekkøy, E. G., & Toussaint, R. 2020, ApJL, 900, L22
Mamajek, E. 2017, RNAAS, 1, 21
Mashchenko, S. 2019, MNRAS, 489, 3003
Masiero, J. 2017, arXiv:1710.09977
McCammon, D., Almy, R., Apodaca, E., et al. 2002, ApJ, 576, 188
Meech, K. J., Hainaut, O. R., & Marsden, B. G. 2004, Icar, 170, 463
Meech, K. J., Weryk, R., Micheli, M., et al. 2017, Natur, 552, 378
Meltzer, B. 1949, Natur, 163, 220
Metzger, A. E., Gilman, D. A., Luthey, J. L., et al. 1983, JGRA, 88, 7731
Micheli, M., Farnocchia, D., Meech, K. J., et al. 2018, Natur, 559, 223
Morbidelli, A., Levison, H. F., Tsiganis, K., & Gomes, R. 2005, Natur, 435, 462
Moro-Martín, A. 2019, ApJL, 872, L32
Moro-Martín, A. 2022, arXiv:2205.04277
Moro-Martín, A., Turner, E. L., & Loeb, A. 2009, ApJ, 704, 733
Mullen, P. D., Cumbee, R. S., Lyons, D., et al. 2017, ApJ, 844, 7

Mullen, P. D., Cumbee, R. S., Lyons, D., & Stancil, P. C. 2016, ApJS, 224, 31
Mumma, M. J., Disanti, M. A., dello Russo, N., et al. 1996, Sci, 272, 1310
Öberg, K. I., Murray-Clay, R., & Bergin, E. A. 2011, ApJL, 743, L16
Opitom, C., Fitzsimmons, A., Jehin, E., et al. 2019, A&A, 631, L8
Price, E. M., Cleeves, L. I., Bodewits, D., & Öberg, K. I. 2021, ApJ, 913, 9
Raymond, S. N., Armitage, P. J., & Veras, D. 2018, ApJL, 856, L7
Raymond, S. N., Kaib, N. A., Armitage, P. J., & Fortney, J. J. 2020, ApJL, 904, L4
Rein, H., Hernandez, D. M., Tamayo, D., et al. 2019, MNRAS, 485, 5490
Rein, H., & Liu, S. F. 2012, A&A, 537, A128
Rubin, M., Altwegg, K., Balsiger, H., et al. 2015, Sci, 348, 232
Rubin, M., Altwegg, K., Balsiger, H., et al. 2018, SciA, 4, eaar6297
Schleicher, D. 1996, IAUC 6333: C/1996 B2 6333, Central Bureau for Astronomical Telegrams
Sekanina, Z. 2019, arXiv:1901.08704
Seligman, D., & Laughlin, G. 2020, ApJL, 896, L8
Seligman, D. Z., Levine, W. G., Cabot, S. H. C., Laughlin, G., & Meech, K. 2021, ApJ, 920, 28
Seligman, D. Z., Rogers, L. A., Cabot, S. H. C., et al. 2022, PSJ, 3, 150
Shakeel, H., Wei, H., & Pomeroy, J. 2018, J. Chem. Thermodyn., 118, 127
Smith, R., Foster, A., & Brickhouse, N. 2012, AN, 333, 301
Stephenson, R. M., & Malanowski, S. 1987, Properties of Organic Compounds (Dordrecht: Springer), 1
Stern, S. A., Slater, D. C., Festou, M. C., et al. 2000, ApJL, 544, L169
Trilling, D. E., Mommert, M., Hora, J. L., et al. 2018, AJ, 156, 261
Tsiganis, K., Gomes, R., Morbidelli, A., & Levison, H. F. 2005, Natur, 435, 459
Wargelin, B. J., Markevitch, M., Juda, M., et al. 2004, ApJ, 607, 596
Wegmann, R., Dennerl, K., & Lisse, C. M. 2004, A&A, 428, 647
Wegmann, R., Schmidt, H., Lisse, C., Dennerl, K., & Englhauser, J. 1998, P&SS, 46, 603
Wisdom, J. 1980, AJ, 85, 1122
Xing, Z., Bodewits, D., Noonan, J., & Bannister, M. T. 2020, ApJL, 893, L48
Yoshida, F., Nakamura, T., Watanabe, J.-I., et al. 2003, PASJ, 55, 701
Zhang, S., Wang, Q. D., Ji, L., et al. 2014, ApJ, 794, 61